Sheet structure in global bifurcations of a driven R-L-diode circuit

Satoshi Tanaka, Shin-ichi Higuchi, and Takashi Matsumoto
Department of Electrical, Electronics, and Computer Engineering, Waseda University, Tokyo, 169, Japan
(Received 16 November 1995)

Sheet structure is found in a global bifurcation diagram of an R-L-diode circuit driven by a sinusoidal voltage source $E\sin 2\pi ft$. Bifurcations of a driven R-L-diode circuit have three interesting features: (1) The alternate appearance of large periodic windows and chaotic bands, where the period of each window increases exactly by one as E is increased. (2) The repeated appearance of period-1 attractors and chaotic bands as E is increased. (3) The existence of two different windows, each of period 2, 3, and 4. This paper attempts to provide a complete understanding of the global nature of the above features. Comprehending global bifurcations of systems, including chaotic behavior, naturally necessitates understanding the nature of stable *and* unstable periodic orbits, the latter being essential in most situations. The R-L-diode circuit is no exception. This paper accomplishes such a task by (i) performing extensive measurements of bifurcations in the (f,E) plane, (ii) simplifying the dynamics of the circuit without losing essential features of the observed bifurcations, and (iii) carefully analyzing the simplified dynamics from a global perspective. An analytical method in this paper is in (iii), where exact bifurcation equations are derived then the bifurcation diagrams are drawn in the $(f,E,S/T)$ space instead of on the (f,E) plane. Here f and E are the frequency and the amplitude of the driving voltage source, and S/T will be precisely defined. This three-dimensional picture reveals the properties of stable and unstable periodic orbits, and makes many of the global bifurcation mechanisms involved almost transparent. In particular, the following are found: (1) All the period-1 attractors and their associated unstable period-1 orbits constitute a sheet structure in the $(f,E,S/T)$ space, and hence belong to the same family. (2) Other periodic attractors of the same period and their associated unstable periodic orbits form a sheet structure in $(f,E,S/T)$ space, and therefore belong to the same respective families. A very good correspondence between the numerical and experimental results is obtained. The global structure revealed will also clarify the global bifurcation mechanisms of other systems, e.g., the gear meshing and the offshore compliant systems described by equations similar to the present system. [S1063-651X(96)14111-8]

PACS number(s): 05.45.+b

I. INTRODUCTION

Consider the R-L-diode circuit given in Fig. 1 driven by the sinusoidal voltage source $E\sin(2\pi ft)$. The dynamics is described by

$$\frac{dq}{dt} = i - g(f(q)),$$
$$L\frac{di}{dt} = -Ri - f(q) + E_b + E\sin(\omega t), \tag{1}$$

where q is the charge stored in the (parasitic) capacitor of the diode, i is the current through the circuit, R and L are the series resistor and the inductor, and E_b is a dc bias. Function g is the well known exponential characteristic of a diode, while f represents the nonlinear characteristic of the capacitive part of the diode. Details of g and f will be discussed in Sec. III.

This circuit exhibits a rich variety of bifurcations, including cascade of period doubling, chaotic attractor [1], intermittency [2], and crisis [3] and many works have reported on this particular circuit [4–25]. Figure 2(a) shows a one parameter bifurcation diagram. The horizontal axis is the amplitude E of the voltage source, and the vertical axis is the current of the circuit sampled at a particular phase of the voltage source. The circuit parameters are $R=75\ \Omega$, $L=2.5$ mH, Diode: 3CC13, dc bias voltage $E_b=0.0$ V, $f=140$ kHz, and $0\leqslant E\leqslant 5.0$ V. [Figure 2(b) will be explained later when we verify the experimental and analytical results.] Note that a bandlike region indicates a chaotic response. One of the first questions is the following: What is responsible for the chaotic behavior when the circuit is so simple and natural? The answer is the nonlinearity of the parasitic capacitor associated with the diode [15]. It has been pointed out [15] that the nonlinearity of the diode capacitor dominates other factors. The resulting model consists of a two-segment, piecewise linear capacitor connected in series with a linear resistor and a linear inductor. The simulation reproduces the experimental results surprisingly well. This (model) circuit still appears to be the simplest nonautonomous circuit which exhibits chaotic behavior.

The next natural question is the following: How are the chaotic attractors formed? The answer is that a significant difference in the vector fields in each of the two regions of the piecewise linear capacitor characteristic gives rise to a ''folding mechanism,'' which in turn is responsible for the

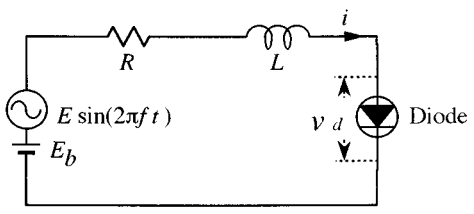

FIG. 1. A driven R-L-diode circuit.

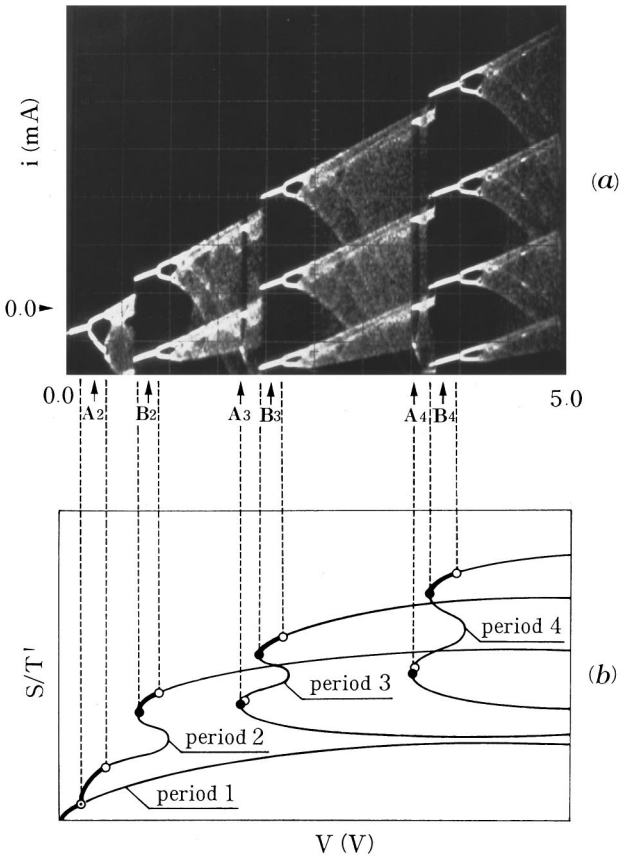

FIG. 2. One parameter bifurcation diagram. (a) Experimental observation. The horizontal axis is the amplitude of the voltage source E (0.5 V/div), the vertical axis is the inductor current i_L (2.0 mA/div), and the source frequency f is 140 kHz. (b) Schematic bifurcation mechanism. A_2 and B_2 indicate two different period-2 attractors. Similarly, A_3 and B_3 (A_4 and B_4) indicate two different period-3 (period-4) windows.

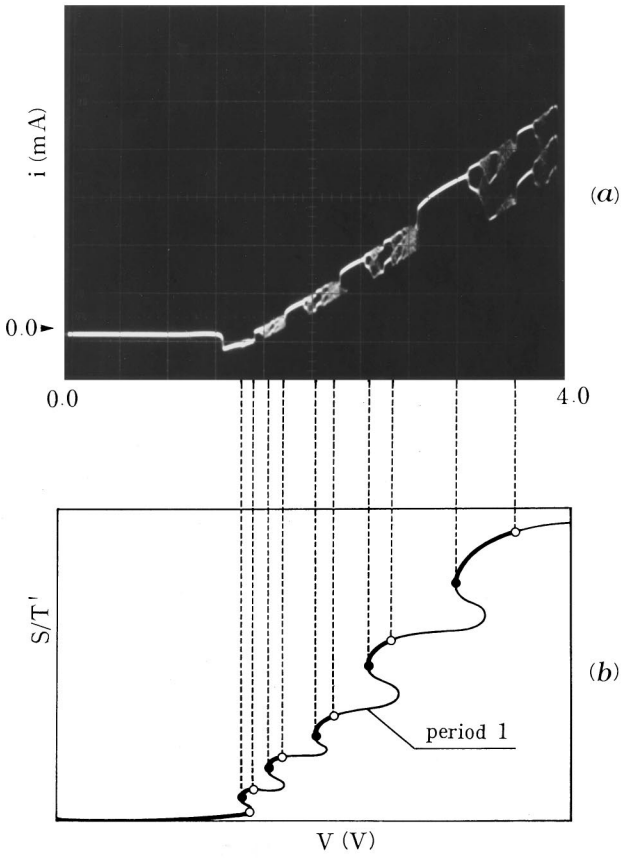

FIG. 3. Another one parameter bifurcation diagram with a different setting. (a) Experimental observation. The source frequency f is 28 kHz, and dc bias E_b is -1.0 V. The horizontal axis is the amplitude of the voltage source E (0.4 V/div), while the vertical axis is the inductor current i_L (2.0 mA/div). (b) Schematic bifurcation mechanism.

chaotic attractor formation [21]. Reduction of the dynamics to a two dimensional discrete dynamical system was a very effective means of analyzing the bifurcations.

The third question is the following: Why does the period of the large periodic window increase by exactly 1? This also is answered in [21].

At lower values of E and f, qualitatively different bifurcations are observed. That is, instead of the increase of the period by 1, a repeated appearance of period-1 attractors are observed sandwiched between chaotic bands [Fig. 3(a)], where parameters are the dc bias voltage $E_b=-1.0$ $Vf=28$ kHz, and $0\leqslant E\leqslant 4.0$ V. [Fig. 3(b) will be explained later]. It was found that the ''multifolding'' mechanism [23] is responsible for this phenomenon. Multifolding is due in turn to the fact that with lower E and f values, the trajectory spends a much longer time in a region (of the state space) where the vector field is fast so that the trajectory rotates more frequently than with larger E and f values. Reduction of the dynamics to a discrete dynamical system is again very useful.

There are at least two more questions which need to be answered:

(i) In Fig. 2, two different period-2 windows denoted by A_2 and B_2 are discernible. Similarly, two different period-3 (period-4) windows denoted by A_3 and B_3 (A_4 and B_4) are observed. How are they related to each other, if indeed they are related?

(ii) What global bifurcation picture incorporates Figs. 2(a) and 3(a), including (i)?

Comprehending global bifurcations including chaotic behavior naturally necessitates understanding the natures of stable *and* unstable periodic orbits, the latter being essential in most situations. The R-L-diode circuit is no exception. This paper accomplishes such a task by (1) extensive mea-

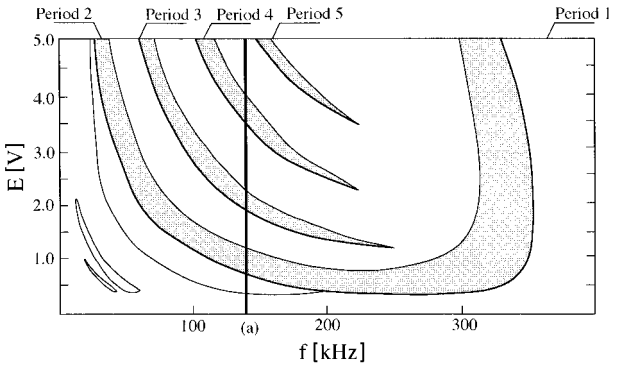

FIG. 4. Observed two parameter bifurcation diagram. The horizontal axis is f:0–400 kHz. The vertical axis is E:0.0–5.0 V (0.0–10.0 V_{pp}).

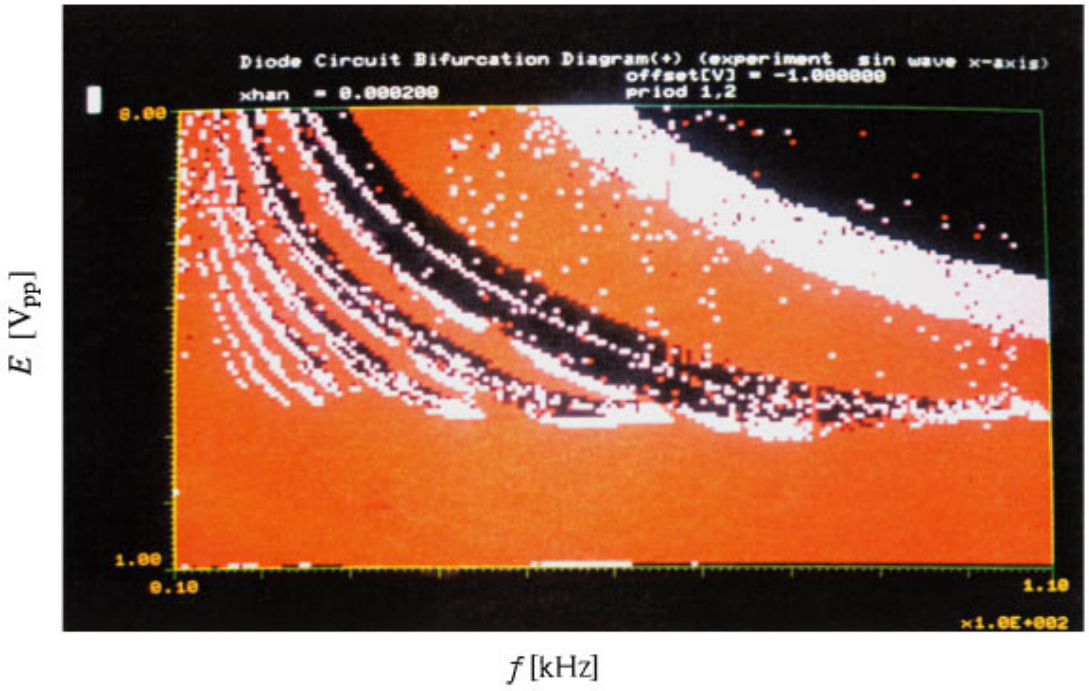

FIG. 5. Another two parameter bifurcation diagram with a different setting. The horizontal axis is f:10–110 kHz. The vertical axis is E:0.5–1.0 V (0.0–8.0 V_{pp}). Red: period-1 attractor. Pink: period-2 attractor. Black: period greater than 2 or chaotic attractor.

suring of the bifurcations in the (f,E) plane, (2) simplifying the dynamics of the circuit without losing essential features of the observed bifurcations, and (3) carefully analyzing the simplified dynamics in a global perspective.

In (3), exact bifurcation equations are derived by taking full advantage of the piecewise linearity with only one break point of the dynamics [24,26]. These bifurcation equations are effectively used to draw bifurcation diagrams in the $(f,E,S/T)$ space instead of on the (f,E) plane, where S and T are the times the trajectory spends in each of the subregions of the piecewise-linear dynamics (see Sec. IV C for a precise definition). As will be shown in Sec. V $(f,E,S/T)$ diagrams reveal the properties of stable and unstable periodic orbits, and make global bifurcation structures almost transparent. Our goal is to explain Figs. 2 and 3 via Fig. 23, a global bifurcation diagram with a sheet structure.

Our results in this paper elucidate several important global bifurcation structures associated with the R-L-diode circuit. In particular, the following are found: (1) The repeatedly observed period-1 attractors and associated unstable period-1 orbits constitute a sheet structure in the $(f,E,S/T)$ space and hence belong to the same family. (2) Other periodic attractors of the same periods and their associated unstable periodic orbits form a sheet structure and belong to the same respective families.

To the best of our knowledge, the first work on R-L-diode bifurcations was by Linsay [4], where period doubling cascade and chaotic attractors were observed. Testa, Perez, and Jeffries [5] then reported a measured Feigenbaum constant which agrees well with the theoretical value 4.6692..., thereby giving evidence of the universality of the Feigenbaum scenario. Rollins and Hunt [6] paid attention to the reverse recovery time of the diode, and proposed an exactly solvable model. Their model, however, cannot be described by a differential equation. It was not still completely clear what was responsible for the chaotic behavior of the R-L-diode circuit. Azzouz, Duhr, and Hasler [10,14], independently of the present authors, proposed a diode model consisting of a piecewise linear resistor and piecewise-linear capacitor and reproduced, by simulation, a bifurcation diagram similar to the observed data. It appeared difficult, however, to perform a detailed analysis because of the two nonlinear elements. Experimental observations similar to our Fig. 2 were reported by Bronson, Dewey, and Linsay [7], Yoon *et al.* [16], Jeffries [17], and Perez [9]. Many discrete mapping models were proposed to reproduce the observed bifurcations (Yoon *et al.* [16], Jeffries [17], and Perez [19]). In most of these models, correspondence between circuit parameters and the parameters of the mapping were not clear. The repeated appearance of period-1 attractors was discussed by Bocko and co-workers [13,22].

We would like to point out that the R-L-diode circuit is not the only one system which is described by an equation of type (1). The first class of problems is the gear meshing vibrations described by [27,28]

$$\frac{d^2x}{dt^2}+C\,\frac{dx}{dt}+h(x)=Bc\omega\,\sin(\omega t)+B\omega^2\cos(\omega t), \quad (2)$$

where x is a dimensionless variable representing the relative angle between the driving and driven gears, c is the damping constant, and h represents (asymmetric) restoration force given by

$$h(x)=\begin{cases} x, & x\geqslant -1 \\ -1, & x<-1. \end{cases} \quad (3)$$

By setting $x_1:=x$, $x_2:=dx/dt$, one sees that Eq. (2) is transformed into

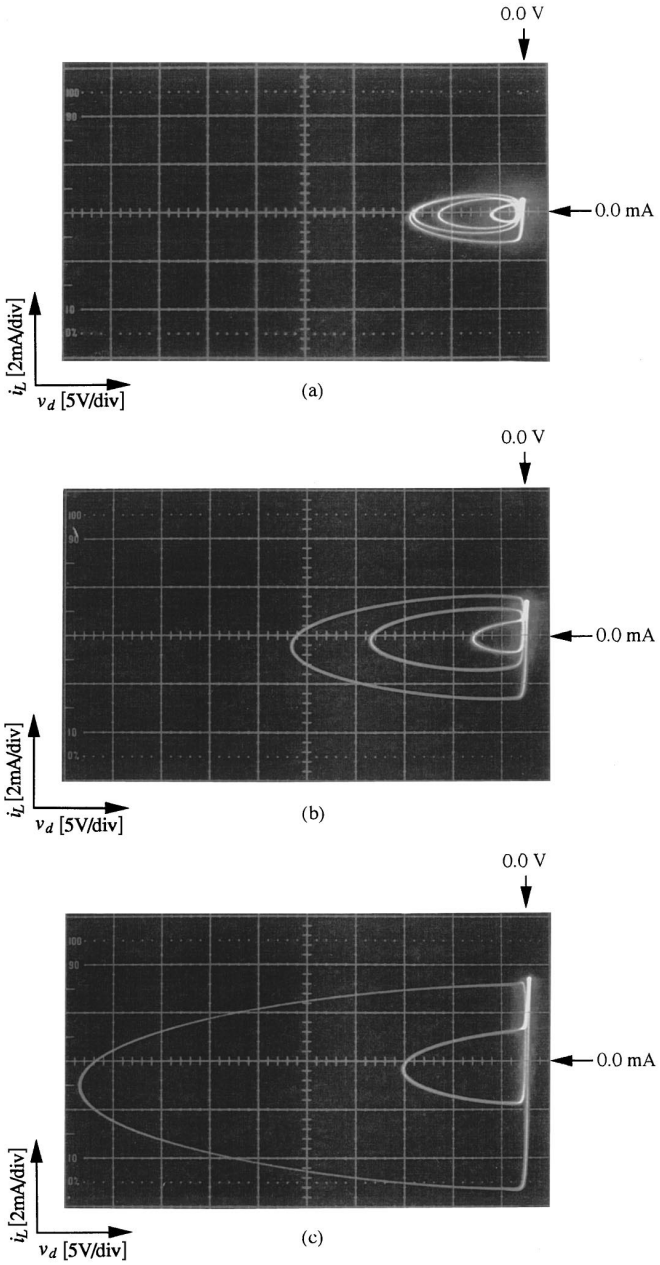

FIG. 6. Orbits of the period-1 attractors. The horizontal axis is the diode voltage v_d (5.0 V/div), and the vertical axis is the inductor current i_L (2.0 mA/div). Since the origin is not located at the center of each figure, the axes are indicated by arrows. $f=30$ kHz. (a) $E=1.9$ V. (b) $E=2.4$ V. (c) $E=2.9$ V.

$$\frac{dx_1}{dt}=x_2,$$
$$\frac{dx_2}{dt}=-cx_2-h(x_1)+Bc\omega\,\sin(\omega t)+B\omega^2\cos(\omega t). \tag{4}$$

The nature of function h is very similar to that of f in Eq. (1) (see Sec. III for details). Bifurcations similar to those of Eq. (1) are observed in Eq. (4), in fact, the ''multifolding'' found in [24] is also observed for Eq. (4), although global bifurcation mechanisms are not well studied in [27,28].

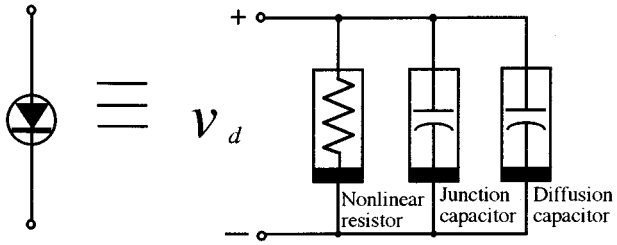

FIG. 7. Equivalent circuit of a (junction) diode.

The second class of problems which are described by equations similar to Eq. (1) is that of compliant off shore structures [29], where the dynamics is given by

$$\eta^2\frac{d^2x}{dt^2}+2\eta\xi\frac{dx}{dt}+\beta(x)x=\sin t,$$
$$\beta(x)=\begin{cases}(1+\sqrt{\alpha})^2/4\alpha, & x>0\\ (1+\sqrt{\alpha})^2/4, & x<0.\end{cases} \tag{5}$$

Here x is the displacement, ξ is the damping ratio with respect to an undamped bilinear frequency obtained by averaging the periodic time, η is the ratio of the forcing frequency to this bilinear frequency, and a is the ratio of the two linear stiffnesses.

That Eq. (1) is similar to those describing other systems is not surprising because the R-L-diode circuit involves no artificial ingredient such as particular nonlinear elements synthesized by engineers; it is a simple series connection of the three extremely natural elements. This appears to be one of the main reasons for the fact that not only engineers [10,14,15,18,21,23–25], but also physicists are interested in this circuit [4–9,11–13,16,17,19,20,22,30]. We suspect that there will be many more natural systems as well which are described by equations similar to Eq. (1).

We close this section by pointing out that the global bifurcation analysis given in this paper is also helpful for possible applications to controlling chaos and chaotic masking systems using the driven R-L-diode circuits [30,31].

II. EXPERIMENTAL OBSERVATIONS OF THE (f,E) PLANE

Figure 4 is a two parameter bifurcation diagram observed on the (f,E) plane. The one parameter bifurcation diagram given in Fig. 2 corresponds to (a), where $f=140$ kHz and $0.0\leqslant E\leqslant 5.0$ V. Observe the shaded areas for the periodic orbits which, explain the large periodic windows of Fig. 2, where the period increases by 1. Note that in Fig. 4, details of the bifurcation structures in the smaller E values are not clearly discernible. This is due to the fact that when E is small, the probed signal is small and the signal-to-noise ratio of the desired signal will deteriorate. Our experience tells us that this is particularly true when f is also small. It will be shown in Sec. IV that adding a negative dc bias has the same effect as decreasing E without deteriorating the signal (see Fig. 1).

Figure 5 shows another observed two parameter bifurcation diagram on the (f,E) plane where 10 kHz$\leqslant f\leqslant$110 kHz,

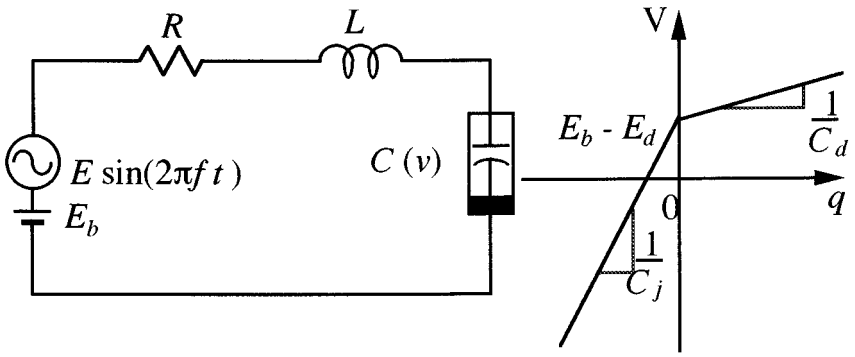

FIG. 8. Simplified equivalent circuit of an R-L-diode circuit.

and 0.5 V$\leqslant E\leqslant$4.0 V (1.0–8.0 V_{pp}, where V_{pp} stands for peak to peak voltage). The following color code is used: red, period-1 attractor; pink, period-2 attractor; and black, period greater than 2 or chaotic attractor. It is readily observed that the pink regions at the lower (f,E) values have essentially the same bananalike shape. The bifurcation diagram in Fig. 3 has dc bias voltage $E_b=-1.0$ V, $f=28$ kHz, and $0\leqslant E\leqslant 4.0$ V. It intersects the bananalike regions of Fig. 5, which explains the alternate appearance of the period-1 attractor and the chaotic band. In order to see the differences of the orbits in different regions, let us observe the trajectories in the ν_d-i plane, where ν_d stands for the diode voltage and i indicates the current. Figure 6 shows these orbits in the three different red regions. Note that all of them are period 1 with respect to the driving source $E\sin 2\pi ft$. However, each trajectory has different ''rotations'' in the (ν_d,i) plane, and the number of rotations is larger for larger E values. This means that the period-1 attractors which are divided by chaotic bands in Fig. 3 have orbits of different types.

III. SIMPLIFICATION OF THE DYNAMICS

In order to carry out a detailed bifurcation analysis, we will simplify the dynamics (1) without losing the essential features of the observed bifurcation structures. As shown in Fig. 7, a very accurate equivalent circuit of a (junction) diode is given by a parallel connection of three nonlinear elements [32]: (1) nonlinear resistor

$$I_d=I_s(\exp(q'\nu/kT)-1), \tag{6}$$

(2) junction capacitor $C_j(\nu)$ due to the depletion region,

$$C_j(\nu)=\begin{cases} C_{j0}(1-\nu/V_{j0})^{-1/2} & \text{when } \nu\leqslant V_{j1} \\ \dfrac{C_{j0}}{2V_{j0}}(1-V_{j1}/V_{j0})^{-3/2}\nu+\dfrac{2V_{j0}-3V_{j1}}{2(V_{j0}-V_{j1})}C_{j0}(1-V_{j1}/V_{j0})^{-1/2} & \text{when } \nu>V_{j1}; \end{cases} \tag{7}$$

and (3) diffusion capacitor $C_d(\nu)$

$$C_d(\nu)=C_{d0}\exp(q'\nu/kT), \tag{8}$$

where I_s, q', k, T, V_{j0}, C_{j0}, C_{d0}, and V_{j1} are the saturation current, electron charge, Boltzmann constant, absolute temperature, potential voltage of the pn junction, junction capacitance at zero bias, diffusion capacitance at zero bias, and turnover voltage between two models of the junction capacitor, respectively.

$C_{j0}(1-\nu/V_{j0})^{-1/2}$ in Eq. (7) is a well known model of the junction capacitor. Observe, however, that this function has a singularity at $\nu=V_{j0}$, i.e., C_j becomes infinite. This model is based on the abrupt space charge edge approximation, and is adequate only for large reverse bias voltages. Thus this model cannot incorporate the forward bias region. Experimental measurements show that, in the forward bias region, the junction capacitance behaves in a rather complicated (nonlinear) manner [33,34]. The second part of Eq. (7) is a reasonable linear approximation in the forward bias region, although it is less well known in device physics and circuit simulations. Since the diffusion capacitance given by

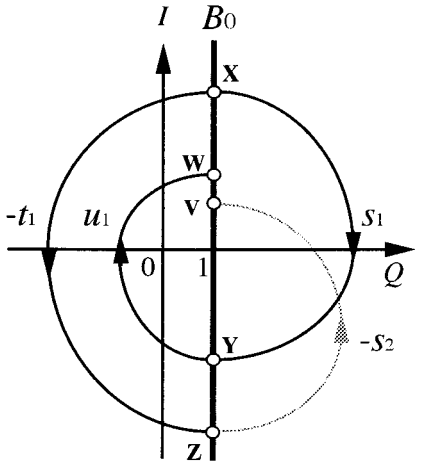

FIG. 9. Schematic of an orbit on the (Q,I) plane. The horizontal axis is I; the vertical axis is Q. B_0 indicates boundary line $Q=1$.

Eq. (8) is dominant for $\nu \geqslant V_{j1}$, the model given at the bottom of Eq. (7) preserves the essential features of the characteristics.

By measurements, the capacitance is found to be 90 nF at 0.5 V (a positive bias) and 235 pF at -1.0 V (a negative bias). Note that the difference in the capacitance values is more than two orders of magnitude. The diode also exhibits the well known rectification characteristic given by Eq. (6). That is, in the reverse bias region the resistance is almost infinite, whereas in the forward bias region the resistance is very small. For example, at 0.5 V the resistance is 100 Ω. By carefully measuring the impedance of the capacitors and the resistor over a frequency range of more than 25 kHz, we found that the impedance of the capacitors is much smaller than that of the resistor. Therefore the diode characteristic can be simplified and can be modeled by a two segment piecewise linear capacitor [15] (see Fig. 8), so that the dynamics of the R-L-diode circuit can be accurately described by

$$\begin{aligned} \frac{dq}{dt} &= i, \\ L\,\frac{di}{dt} &= -Ri - \begin{cases} \dfrac{1}{C_d}\,q & \text{if } q \geqslant 0 \\ \dfrac{1}{C_j}\,q & \text{if } q < 0 \end{cases} - E_d + E_b \\ &\quad + E\,\sin(\omega t), \end{aligned} \tag{9}$$

where C_d is the diffusion capacitance at 0.5-V bias, C_j is the junction capacitance at -1.0-V bias, $E_d = 0.5$ V is the break point voltage at which the capacitance value changes between the junction capacitance and the diffusion capacitance, i is the circuit current, and q is the charge stored in the capacitor. Note that the bias E_b is also included. One can explain Fig. 6 in terms of C_d and C_j: with a smaller E, the trajectory spends more time in the C_j region than in the C_d region. This, in turn, explains the larger number of rotations with a smaller E, because the resonant frequency of the C_j region is higher than that of the C_d region.

IV. EXACT BIFURCATION EQUATIONS

In this section, we will derive the exact bifurcation equations of the simplified dynamics (9) by taking full advantage of the piecewise linearity, i.e., that the dynamics consists of two linear differential equations connected at the boundary $q = 0$. Using these equations, one cannot only identify various bifurcation sets but can also construct a three dimensional bifurcation diagram of periodic orbits, which clarifies the local and global structures of periodic windows.

We first rescale the dynamics (9) and convert it into a fourth order autonomous system as follows:

$$\begin{aligned} \frac{dQ}{d\tau} &= I, \\ \frac{dI}{dt} &= -kI - \begin{cases} \dfrac{1}{C_j}\,Q & \text{if } Q < 1 \\ \dfrac{1}{C_d}\,Q + \dfrac{1}{C_d}\,\dfrac{1}{C_j} & \text{if } Q \geqslant 1 \end{cases} \\ &\quad + \frac{E}{C_d(E_b - E_d)}\,M, \\ \frac{dM}{d\tau} &= N, \\ \frac{dN}{d\tau} &= -M, \end{aligned} \tag{10}$$

where

$$Q \equiv \frac{\omega^2 L}{C_j(E_b - E_d)}\,q + 1, \quad I \equiv \frac{\omega L}{C_j(E_b - E_d)}\,i, \quad \tau \equiv \omega t,$$

$$k \equiv \frac{R}{\omega L}, \quad \frac{1}{C_x} \equiv \frac{1}{\omega^2 C_x L}\ (x = d, j),$$

$$M^2 + N^2 = 1.$$

Since $E_d < 0$, it follows from Eq. (10) that adding a negative bias E_b has the effect of decreasing the magnitude of E. Note that the sinusoidal voltage source has been converted into a harmonic oscillator $dM/d\tau = N$, $dN/d\tau = -M$. Equation (10) is a two region piecewise linear vector field on $\mathbb{R}^4$, which is most conveniently recast as

$$\frac{dx}{d\tau} = \begin{cases} Ax & (Q \geqslant 1) \\ Bx + p & (Q < 1), \end{cases} \tag{11}$$

where

$$x = (Q, I, M, N)^T, \quad p = \left(0, \frac{1}{C_d} - \frac{1}{C_j}, 0, 0\right)^T$$

(T indicates the transpose of a vector),

$$A = \begin{bmatrix} 0 & 1 & 0 & 0 \\ -\dfrac{1}{C_j} & -k & \dfrac{E}{C_j(E_b - E_d)} & 0 \\ 0 & 0 & 0 & 1 \\ 0 & 0 & -1 & 0 \end{bmatrix},$$

$$B = \begin{bmatrix} 0 & 1 & 0 & 0 \\ -\dfrac{1}{C_d} & -k & \dfrac{E}{C_j(E_b - E_d)} & 0 \\ 0 & 0 & 0 & 1 \\ 0 & 0 & -1 & 0 \end{bmatrix}.$$

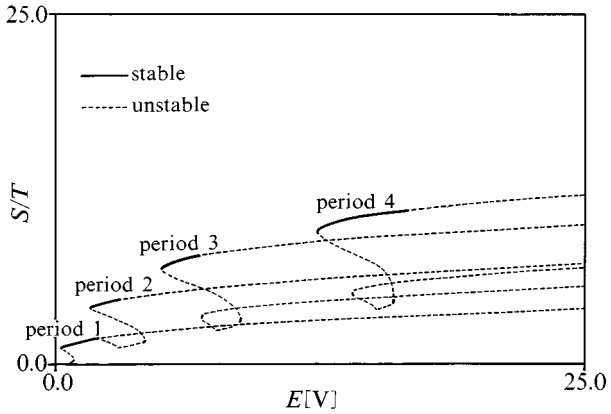

FIG. 10. $(E,S/T)$ diagram.

We will use Eq. (11) extensively to perform various bifurcation analyses in the next section.

A. Characterization of periodic orbits

Figure 9 shows a schematic of an orbit on the (Q,I) plane. Consider a point $\mathbf{X}$ lying on the boundary B_0 defined by $Q=1$. Let $\mathbf{Y}$ and $\mathbf{Z}$ be the points where the trajectory starting from $\mathbf{X}$ hits B_0 again at positive time s_1 and negative time $-t_1$. Similarly, let $\mathbf{W}$ be the point where the trajectory starting from $\mathbf{Y}$ hits B_0 again at a positive time u_1. Since the system is linear in each region, we have

$$\mathbf{Y}=\mathbf{e}^{Ds_1}\mathbf{X},$$

$$\mathbf{Z}=\mathbf{e}^{-At_1}\mathbf{X},$$

$$\mathbf{W}=\mathbf{e}^{Au_1}\mathbf{Y}=\mathbf{e}^{Au_1}\mathbf{e}^{Ds_1}\mathbf{X},$$

where

$$\mathbf{D}=\mathbf{A}^{-1}\mathbf{B}\mathbf{A},$$

and $\mathbf{e}^{-At_1}$ stands for the matrix exponential of $-\mathbf{A}t_1$. Other symbols have similar meanings. Since $\mathbf{X}$, $\mathbf{Y}$, and $\mathbf{W}$ all lie on the boundary B_0,

$$\langle\alpha,\mathbf{X}\rangle=1,\quad \langle\alpha,\mathbf{e}^{Ds_1}\mathbf{X}\rangle=1,$$

$$\langle\alpha,\mathbf{e}^{-At_1}\mathbf{X}\rangle=1,\quad \langle\alpha,\mathbf{e}^{Au_1}\mathbf{e}^{Ds_1}\mathbf{X}\rangle=1,$$

where $\langle\,,\rangle$ denotes the ordinary inner product on $\mathbb{R}^4$ and $\alpha=(1,0,0,0)^T$. Therefore

$$\mathbf{X}=(\mathbf{e}_1\alpha^T+\mathbf{e}_2\alpha^T\mathbf{e}^{Ds_1}+\mathbf{e}_3\alpha^T\mathbf{e}^{-At_1}+\mathbf{e}_4\alpha^T\mathbf{e}^{Au_1}\mathbf{e}^{Ds_1})^{-1}(1,1,1,1), \tag{12}$$

where

$$\mathbf{e}_1=(1,0,0,0)^T,\quad \mathbf{e}_2=(0,1,0,0)^T,\quad \mathbf{e}_3=(0,0,1,0)^T,$$

$$\mathbf{e}_4=(0,0,0,1)^T.$$

If the trajectory starting from $\mathbf{Z}$ hits point $\mathbf{V}$ on the boundary B_0 at a negative time $-s_2$, then $\mathbf{V}$ is given by

$$\mathbf{V}=\mathbf{e}^{-Ds_2}\mathbf{Z}=\mathbf{e}^{-Ds_2}\mathbf{e}^{-At_1}\mathbf{X}.$$

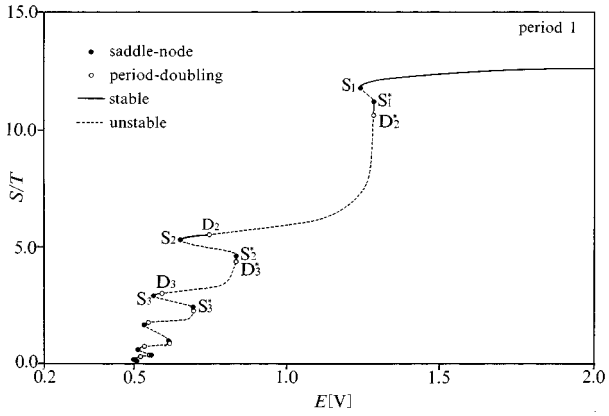

FIG. 11. $(E,S/T)$ diagram for a period-1 orbit at $f=30$ kHz.

If this orbit is periodic, then $\mathbf{W}=\mathbf{V}$, which is equivalent to

$$(\mathbf{e}^{Au_1}\mathbf{e}^{Ds_1}-\mathbf{e}^{-Ds_2}\mathbf{e}^{-At_1})\mathbf{X}=\mathbf{0}.$$

Consequently, a periodic orbit is characterized by

$$(\mathbf{e}^{Au_1}\mathbf{e}^{Ds_1}-\mathbf{e}^{-Ds_2}\mathbf{e}^{-At_1})\mathbf{k}(s_1,t_1,u_1)\mathbf{h}=\mathbf{0}, \tag{13}$$

$$\{\mathbf{e}_3\mathbf{k}(s_1,t_1,u_1)\mathbf{h}\}^2+\{\mathbf{e}_4\mathbf{k}(s_1,t_1,u_1)\mathbf{h}\}^2=1, \tag{14}$$

where [see Eq. (12)] $\mathbf{k}(s_1,t_1,u_1)=(\mathbf{e}_1\alpha^T+\mathbf{e}_2\alpha^T\mathbf{e}^{Ds_1}+\mathbf{e}_3\alpha^T\mathbf{e}^{-At_1}+\mathbf{e}_4\alpha^T\mathbf{e}^{Au_1}\mathbf{e}^{Ds_1})^{-1}$ and $\mathbf{h}=(1,1,1,1)$. Note that there are only three (out of four) independent equations in Eq. (13) because the third and fourth components of $\mathbf{W}$ and $\mathbf{V}$ are dependent through Eq. (14).

B. Exact bifurcation equations of periodic orbits

Reference [26] rigorously shows that eigenvalues of the Poincare return map on B_0 are given by the eigenvalues of the 4×4 matrix

$$\Phi=\mathbf{e}^{At_1}\mathbf{e}^{Ds_2}\mathbf{e}^{Au_1}\mathbf{e}^{Ds_1}.$$

One of the four eigenvalues of Φ is always 1 because M and N constitute a harmonic oscillator [see Eq. (10)]. If $\mathbf{X}$ is a periodic point, one of the remaining three eigenvalues is also 1. Note that a saddle node bifurcation (period doubling bifurcation) is characterized by the fact that one of the remaining two eigenvalues is 1 (-1). Therefore, saddle node and period doubling bifurcations are characterized, by the following: saddle node bifurcation,

$$3-\mathrm{Tr}(\Phi)+\mathrm{Det}(\Phi)=0,$$

$$(\mathbf{e}^{Au_1}\mathbf{e}^{Ds_1}-\mathbf{e}^{-Ds_2}\mathbf{e}^{-At_1})\mathbf{k}(s_1,t_1,u_1)\mathbf{h}=0, \tag{15}$$

$$\{\mathbf{e}_3\mathbf{k}(s_1,t_1,u_1)\mathbf{h}\}^2+\{\mathbf{e}_4\mathbf{k}(s_1,t_1,u_1)\mathbf{h}\}^2=1,$$

and period doubling bifurcation,

$$-1-\mathrm{Tr}(\Phi)+\mathrm{Det}(\Phi)=0,$$

$$(\mathbf{e}^{Au_1}\mathbf{e}^{Ds_1}-\mathbf{e}^{-Ds_2}\mathbf{e}^{-At_1})\mathbf{k}(s_1,t_1,u_1)\mathbf{h}=0, \tag{16}$$

$$\{\mathbf{e}_3\mathbf{k}(s_1,t_1,u_1)\mathbf{h}\}^2+\{\mathbf{e}_4\mathbf{k}(s_1,t_1,u_1)\mathbf{h}\}^2=1,$$

where $\mathrm{Tr}(\Phi)$ is the trace of Φ, and $\mathrm{Det}(\Phi)$ is the determination of Φ.

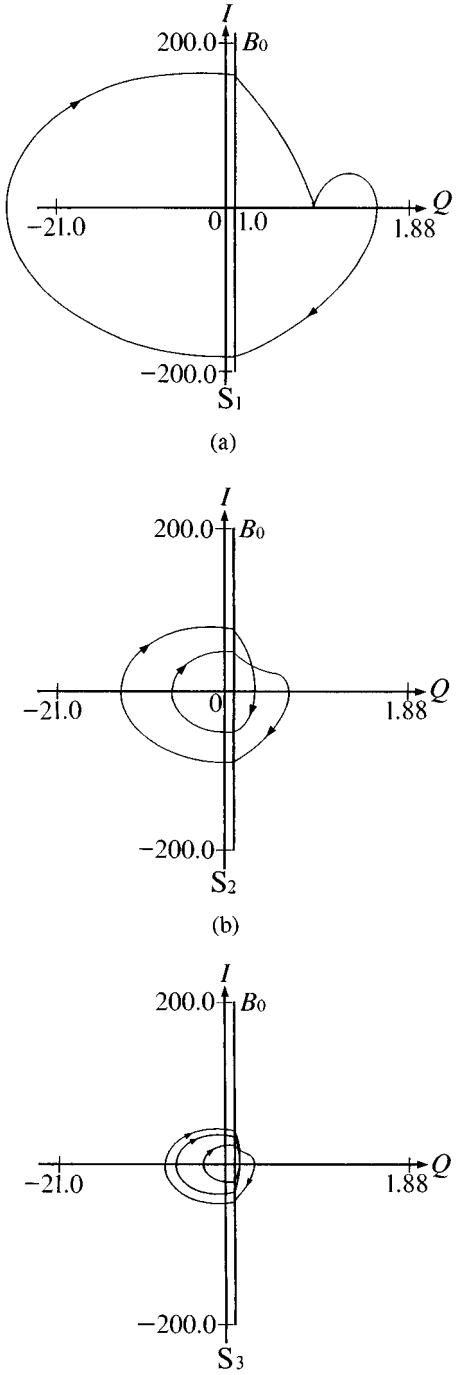

FIG. 12. Period-1 orbits on the (Q,I) plane. (a) Orbit corresponding to S_1 in Fig. 11. (b) Orbit corresponding to S_2 in Fig. 11. (c) Orbit corresponding to S_3 in Fig. 11.

Other types of periodic orbits can be characterized similarly. These exact bifurcation equations will be used extensively and will play fundamental roles in the rest of this paper. We should emphasize that no integration formula (e.g., the Runge-Kutta formula) will be used in obtaining the bifurcation diagrams. The bifurcation diagrams will be obtained simply by solving Eqs. (15) and (16) (via Euler). This method is particularly powerful when we compute an unstable (saddle type) periodic orbit with many rotations, because the error incurred by the Runge-Kutta formula significantly deteriorates accuracy. In fact, some of the complicated

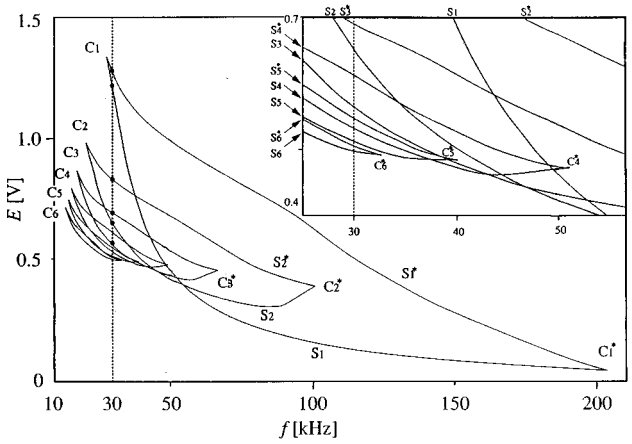

FIG. 13. (f,E) diagram for period-1 orbits.

saddle type periodic orbits cannot be captured by the Runge-Kutta formula.

Of course, saddle node as well as period doubling bifurcations cannot be completely characterized solely by eigenvalue conditions. In most experimental (numerical) studies, however, eigenvalue conditions suffice.

C. New variable S/T

Even with the exact bifurcation equations derived in Sec. IV B, it is still difficult to explain the structures in the observed bifurcation diagrams, Figs. 2, 3, 4, and 5. A crucial step here is to choose another variable for bifurcation diagrams, in addition to f and E. In Ref. [26], one of the state variables is chosen as the third variable. In the R-L-diode circuit, however, our extensive simulations indicate that the state variables are not suitable for explaining the bifurcations of interest because the resulting bifurcation curves give rise to many self-intersection points. This appears to be attributable to the fact that the coordinates of the state variables at a particular cross section ''move around'' as parameters are varied.

As was pointed out at the end of Sec. III, the time which a trajectory spends in the C_j region plays an important role in characterizing a trajectory. In order to account for this, let S be the time a trajectory spends in the C_d region (i.e., $Q \geqslant 1$), let T be the time a trajectory spends in the C_j region $(Q<1)$, and consider S/T $(S+T=2\pi)$. It turns out that this is a very good choice for the third variable. Figure 10 shows a one parameter bifurcation diagram for period-1, -2, -3, and -4 orbits obtained by solving the exact equations. The circuit parameters are

$$R=214\ \Omega,\ L=2.5\ \text{mH},\ C_j=235\ \text{pF},\ C_d=51.4\ \text{nF},$$

$$f=150\ \text{kHz},\ E_b=-1.0\ \text{V}.$$

The horizontal axis is the voltage source amplitude E, while the vertical axis is S/T. The solid curves (broken curves) indicate that the orbits are stable (unstable). In Sec. V, we will perform a detailed bifurcation analysis on each of the periodic orbits given in Fig. 10, and then elucidate a global picture.

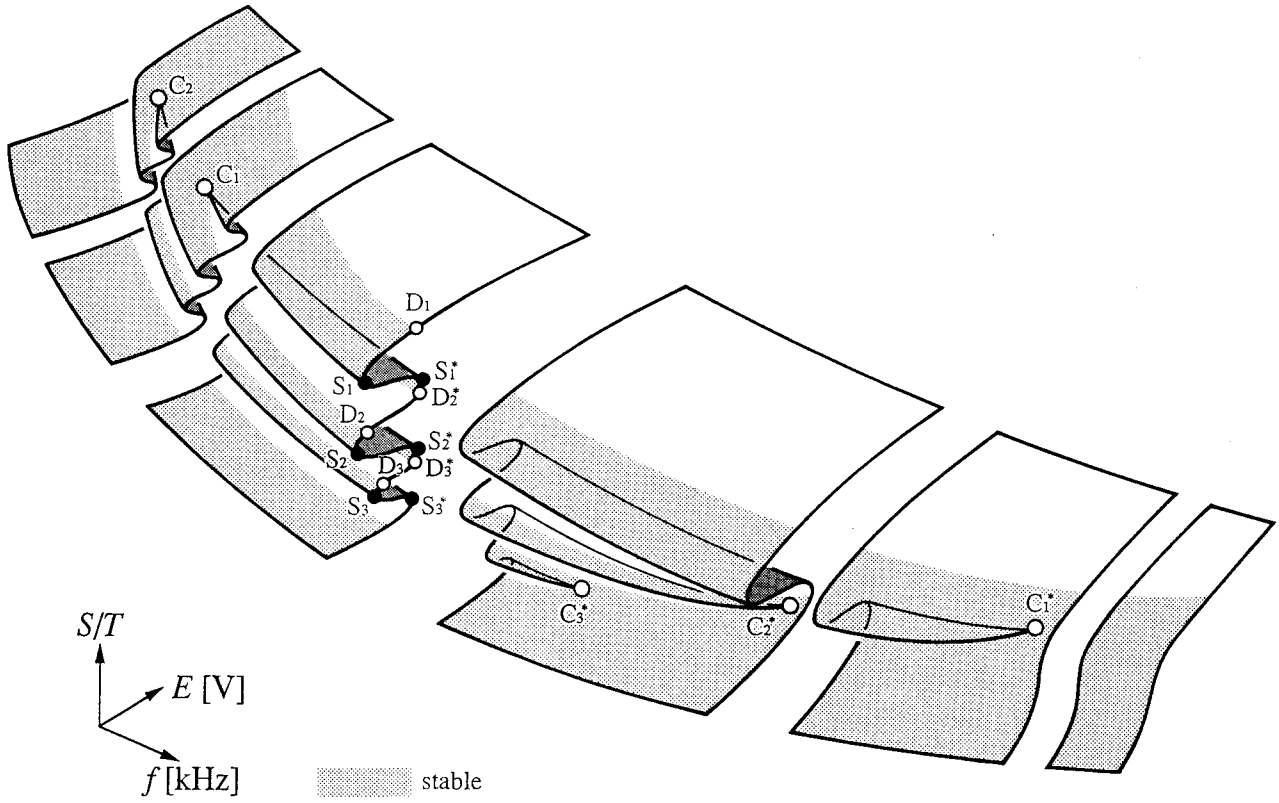

FIG. 14. A schematic $(f,E,S/T)$ diagram for period-1 orbits.

V. BIFURCATION STRUCTURE IN $(f,E,S/T)$ SPACE

With exact bifurcation equations at hand, this section is devoted to a detailed bifurcation analysis. Particular attention is paid to those properties of unstable periodic orbits that are related to the sheet structure. The goal of this section is to explain Figs. 2 and Fig. 3 using Fig. 23.

A. Period-1 orbits

Figure 11 shows one parameter bifurcation diagrams for a period-1 orbit that are obtained by solving Eqs. (13) and (14). The circuit parameters are

$$R=214\ \Omega,\ L=2.5\ \text{mH},\ C_j=235\ \text{pF},$$

$$C_d=51.4\ \text{nF},\ E_b=-1.0\ \text{V},\ f=30\ \text{kHz}.$$

The horizontal axis is the amplitude E of the voltage source while the vertical axis is S/T. A solid (broken) line indicates that the period one orbit is stable (unstable). Symbol S, associated with a black circle (D is associated with a white circle), indicates a point where saddle node (period doubling) bifurcation takes place. Subscripts 1, 2, and 3 are only for distinguishing the bifurcation points. The distinction between S_n and S_n^* is that, at S_n, a pair of periodic orbits is born as E is increased, while, at S_n^*, a pair of periodic orbits disappears as E is increased. The distinction between D_n and D_n^* lies in the fact that D_n is associated with S_n, while D_n^* is associated with S_n^*. The bifurcation structures of interest are clearly captured: all the period-1 orbits belong to the same family in the parameter space. In Fig. 11, for example, bifurcations take place repeatedly as S/T increases: saddle node bifurcation $(S_2)\rightarrow$stable period-1 orbit (solid line)$\rightarrow$period doubling bifurcation $(D_2)\rightarrow$unstable period-1 orbit (broken line)$\rightarrow$reverse period doubling bifurcation $(D_2^*)\rightarrow$stable period-1 orbit (solid line)$\rightarrow$saddle node bifurcation (S_1^*).

The nature of the period-1 orbits, however, varies as S/T varies. Specifically, the number of rotations increases as S/T decreases, as shown in Fig. 12, where the trajectories are shown on the Q-I plane. The negative Q axis has a different scale from that of the positive-Q axis. This is to avoid drawing large ''semicircles'' on the half plane $Q<0$. The orbit in Fig. 12(a) correspond to S_1 in Fig. 11. Similarly, Fig. 12(b) corresponds to S_2 in Fig. 11. Note that a periodic orbit becomes more complicated as the time which the orbit spends in the C_j region increases. However, there is a limit to this. If S/T is very small, the orbit stays in the C_j region all the time [at least in the piecewise linear model Eq. (9)], and it is not complicated at all.

Compared with the trajectories on the Q-I plane (see Fig. 12), the experimentally observed trajectories in the ν_d-i plane are strongly compressed against the i axis (see Fig. 6), because C_d is much larger than C_j. However, the correspondence between Figs. 6 and 12 is clear. The stability interval between D_2^* and S_1^* is extremely narrow; therefore, it is very difficult to observe the period-1 attractor in this particular interval in an experiment. In contrast, the stability interval between S_2 and D_2 is so large that the period-1 attractor in this interval can easily be observed in an experiment (see Fig. 3).

Figure 13 shows saddle node bifurcation sets in the (f,E) two parameter plane. The vertical axis is the frequency f and

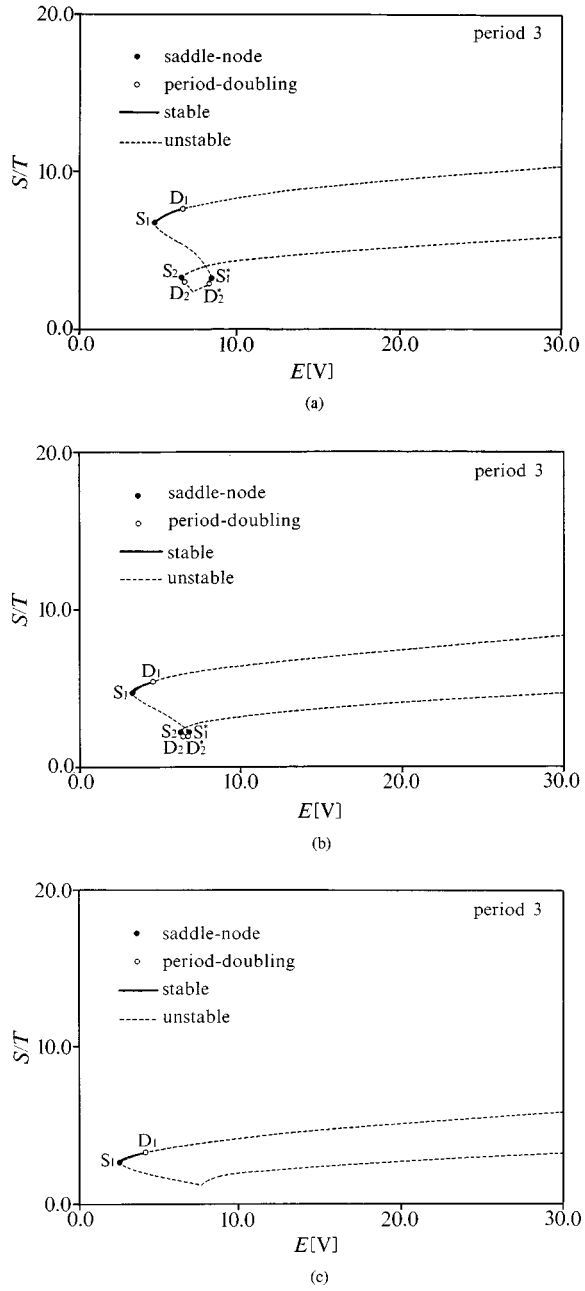

FIG. 15. $(E,S/T)$ diagram for period-3 orbits. (a) $f=150$ kHz, (b) $f=200$ kHz, and (c) $f=300$ kHz.

the horizontal axis is the amplitude E of the voltage source. In Fig. 13, curves S_n and S_n^* indicate saddle node bifurcation sets that correspond to those in Fig. 11. The straight dotted line at 30 kHz corresponds to Fig. 11. The S_n and S_n^* pair meets and vanishes at points C_n and C_n^*. Those points are often called the cusp points [26].

Now let us compare Fig. 13 with the experimental data in Fig. 5. First recall the color code: pink, period 1; red, period 2; and black, period greater than 2 or chaotic. Since in an experiment we can observe attractors only, we note that a boundary between the pink and the red regions signifies period doubling bifurcations, while Fig. 13 shows saddle node bifurcation sets. Still we observe the bananalike regions in both figures. This is attributable to the fact that each saddle node bifurcation set S_n always accompanies a period doubling bifurcation set D_n, which is clear from Fig. 11. Note that, in Fig. 5, a boundary between the pink and black regions signifies period doubling bifurcations of period-2 orbits. Note also that a boundary between the black and red regions signifies saddle node bifurcations of period one orbits.

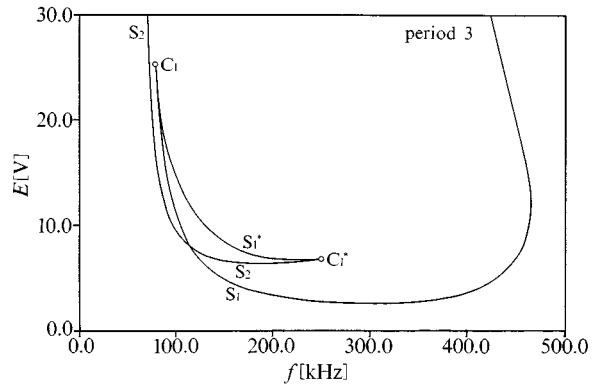

FIG. 16. (f,E) diagram for period-3 orbits.

Even though Fig. 13 explains why one observes Fig. 5 experimentally, it still does not explain how the periodic orbits of interest are connected with each other. In order to observe this more transparently, all the information concerning the period-1 orbits obtained so far are combined, and a schematic three dimensional bifurcation diagram consistent with the data is shown in Fig. 14. However, some of the values of S_n and D_n shown in Figs. 11 and 13 are not shown in Fig. 14 since the picture becomes too complicated to draw. The sheetlike object is the set of periodic orbits in the $(f,E,S/T)$ space together with stability information. The shaded region of the sheet indicates the stable period-1 orbit; the nonshaded regions indicate an unstable period-1 orbit. It can be observed that all the period-1 attractors belong to the wavy sheet. Thus it is clear that all the period-1 attractors belong to the same family in the (f,E) parameter plane.

B. Period-3 orbits

The bifurcation structure of period-2 orbits is rather complicated, so let us explain the bifurcation structures of period-3 and -4 orbits before explaining the bifurcation structure of the period-2 orbits. Figure 15 shows one parameter bifurcation diagrams for a period-3 orbit computed by solving the bifurcation equations described in Sec. IV. The frequencies are (a) $f=150$ kHz, (b) $f=200$ kHz, and (c) $f=300$ kHz. Other circuit parameters are the same as those for period-1 orbits. The horizontal axis is the amplitude E of the voltage source, and the vertical axis is S/T. A solid line (broken line) represents that the period-3 orbits are stable (unstable); S_n and S_n^* (black circles) indicate saddle node bifurcations, and D_n and D_n^* (white circles) indicate period doubling bifurcations. Contrary to the bifurcation diagrams of the period-1 orbits, the bifurcation diagram is not monotone with respect to S/T. There is a self-intersecting point. However, this singular point does not have any special physical meaning.

Three periodic windows, S_1-D_1, S_2-D_2, and D_2^*-S_1^*, can be observed in Fig. 15(a). The windows S_2-D_2 and

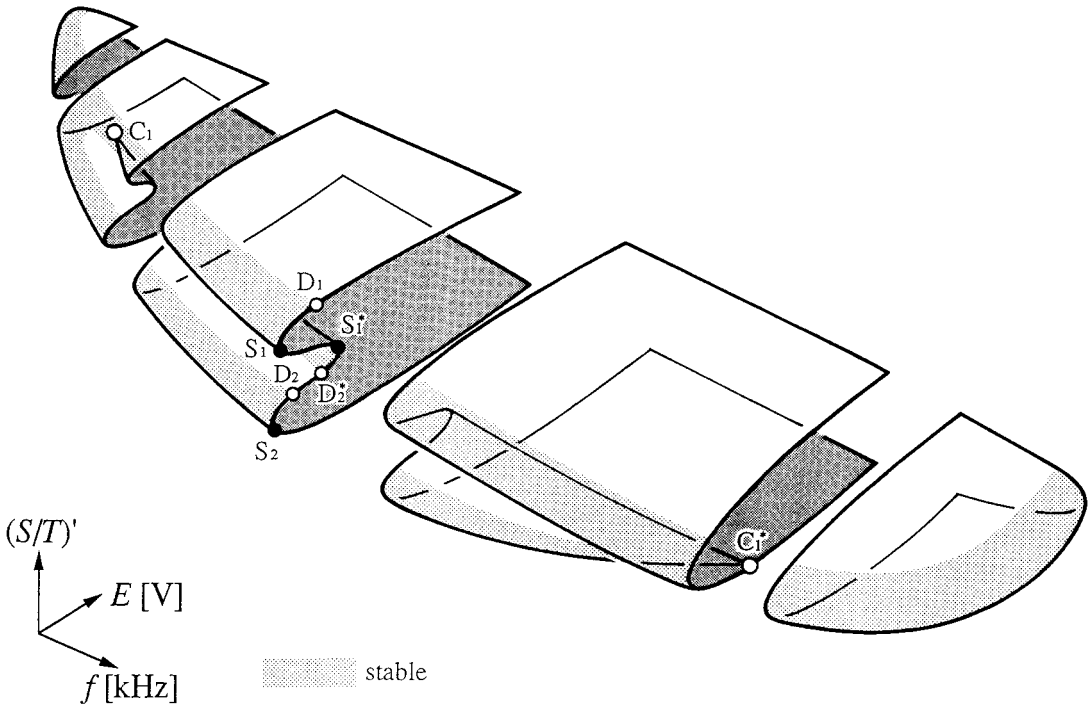

FIG. 17. A schematic $(f,E,(S/T)')$ diagram for period-3 orbits.

D_2^*-S_1^* are small, compared with the window S_1-D_1. Recall Fig. 2, in which the two different period three attractors indicated by A_3 and B_3 are discernible. We observe that A_3 and B_3 correspond to the windows S_2-D_2 and S_1-D_1. As f is increased, the two small windows S_2-D_2 and D_2^*-S_1^* become smaller and closer to each other [see Fig. 15(b)]. Finally, these two windows collide and vanish [see Fig. 15(c)]. Let us next check how these saddle node bifurcation sets look in the (f,E) two parameter plane (Fig. 16). The vertical axis is the frequency f, and the horizontal axis is the amplitude E of the voltage source. Note that there are two cusp points where two saddle node bifurcation sets merge. Now we realize that Fig. 15, which is an $(E,S/T)$ diagram, together with Fig. 16, which is an (f,E) diagram, still do not sufficiently clarify the bifurcation structure. If we look at these bifurcations in the $(f,E,S/T)$ space, however, then they are almost transparent. Before explaining the $(f,E,S/T)$ diagram, let us recall that there are self-intersection points in Figs. 15(a) and 15(b) and that they do not have any significant physical meaning. Figure 17 is a schematic bifurcation diagram consistent with the above data. This schematic diagram ''unfolds'' the self-intersection points in order to make the picture more transparent. The new coordinate is called $(S/T)'$ instead of (S/T). The $(f,E,(S/T)')$ diagram again consists of a two-dimensional, sheetlike object where the shaded area indicates stable period-3 orbits. The windows S_2-D_2 and D_2^*-S_1^* are omitted from Fig. 17 since they are too small to draw. It is seen immediately that all period-3 windows S_2-D_2, S_1-D_1, and D_2^*-S_1^* belong to the same family. In particular, the windows corresponding to A_3 and B_3 observed in Fig. 2 belong to this family.

C. Period-4 orbits

The bifurcation structures of the period four orbits are similar to those of period-3 orbits. Figure 18 shows one parameter bifurcation diagrams with the frequencies (a) $f=150$ kHz and (b) $f=300$ kHz. At $f=150$ kHz, there are three periodic windows. As f increases, two small windows S_2-D_2 and D_2^*-S_1^* become smaller and closer to each other. Finally,

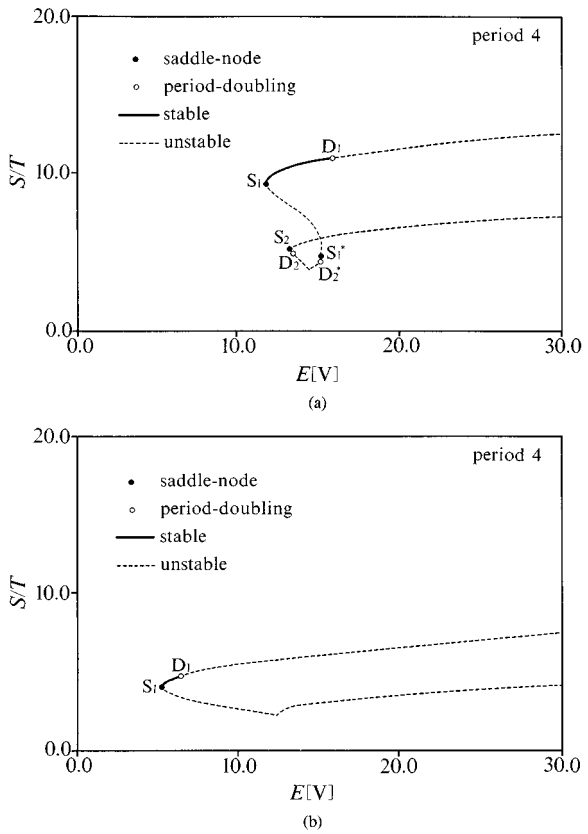

FIG. 18. $(E,S/T)$ diagram for period-4 orbits. (a) $f=150$ kHz. (b) $f=300$ kHz.

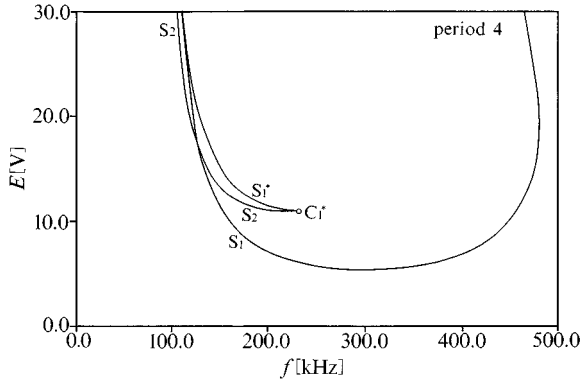

FIG. 19. (f,E) diagram for period-4 orbits.

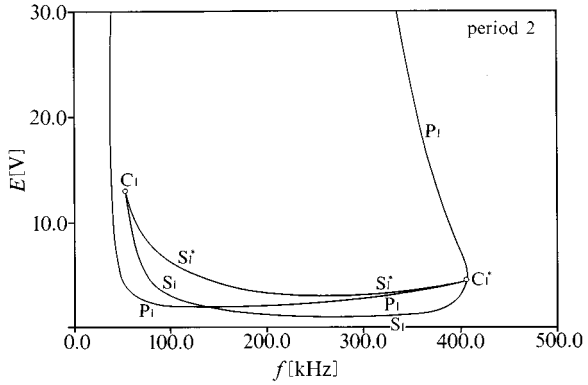

FIG. 21. (f,E) diagram for period-2 orbits.

they collide and vanish [see Fig. 18(b)]. Figure 19 shows the saddle node bifurcation sets on the (f,E) plane. We omit the schematic model since it is basically the same as that in Fig. 17. We can see that the two period-4 windows in Fig. 2 indicated by A_4 and B_4 correspond to S_2-D_2 and S_1-D_1 [Fig. 18(a)].

D. Period-2 orbits

The bifurcation structures of the period-2 orbits have several features which are very different from those of other periodic orbits. While all other periodic orbits are born out of saddle node bifurcations, some of the period-2 orbits are born out of period doubling bifurcations of period-1 orbits.

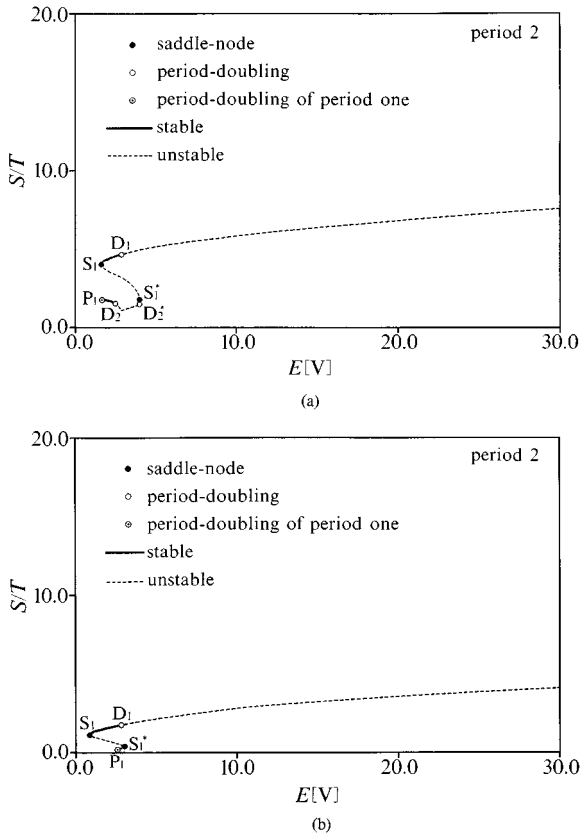

FIG. 20. $(E,S/T)$ diagram for period-2 orbits. (a) $f=150$ kHz. (b) $f=300$ kHz.

Figure 20 shows one parameter bifurcation diagrams of the period-2 orbits. The frequencies are (a) $f=150$ kHz, (b) $f=200$ kHz, and (c) $f=300$ kHz. Other circuit parameters are the same as those for the period one orbits. The horizontal axis is the amplitude E of the voltage source and the vertical axis is S/T. A solid line (broken line) represents the fact that the period-2 orbits are stable (unstable), and S_n (S_n^*) (black circles) and D_n (D_n^*) (white circles) indicate points where period-2 saddle node bifurcation and period doubling bifurcation take place. The symbol P_n (the white circles with dot) stands for a point where period doubling bifurcation of the period-1 orbit occurs. P_1 is the same set that is symbolized as D_1 in Fig. 11. Note that there are three stable regions of period-2 orbits in Fig. 20(a): S_1-D_1, P_1-D_2, and D_2^*-S_1^*. Regions P_1-D_2 and D_2^*-S_1^* are small compared with the window S_1-D_1. As f increases, the two small regions P_1-D_2 and D_2^*-S_1^* become smaller and move closer to each other [see Fig. 20(b)]. However, they never collide with each other. Finally, the regions S_1-D_1 and D_2^*-S_1^* collide with each other (instead of the pair P_1-D_2 and D_2^*-S_1^*) and vanish. Figure 21 shows the situation on the (f,E) plane where the horizontal axis is the frequency and the vertical axis is the amplitude of the voltage source. At the cusp points C_1 and C_1^*, the saddle node bifurcation sets S_1^* and S_1 become tangent to each other and vanish. In the area around the cusp point C_1^*, the bifurcation structure is rather complicated. Figure 22 shows a schematic $(f,E,(S/T)')$ diagram of the period-2 orbits. Note that the period doubling bifurcation set of period-1 orbits P_1 is not tangent to the saddle node bifurcation set at C_1^*. It is clearly shown that two types of period-2 orbits which have different origins are in the same family on the (f,E) plane. In terms of Fig. 2, the stable period-2 interval A_2 is born out of period doubling (of a period-1 orbit), while window B_2 is result of a saddle node bifurcation, and yet they belong to the same family of period-2 orbit.

E. Global bifurcation structure

We are now ready to see all the bifurcation structures explained above in a single picture. Figure 23 is a schematic $(f,E,(S/T)')$ diagram of global bifurcation structure. The color code is as follows: green, period 4; purple, period 3; yellow, period 2; and blue, period 1. The light colored region

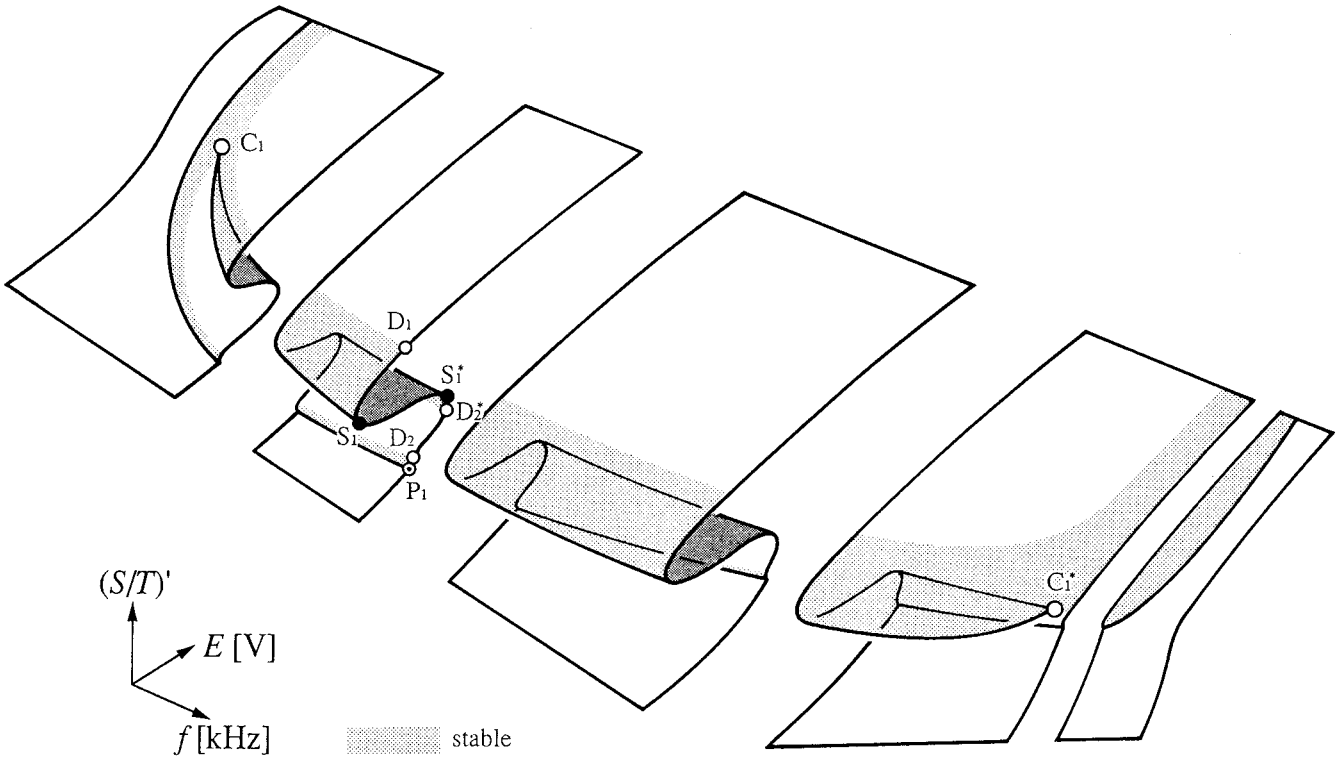

FIG. 22. A schematic model $(f,E,(S/T)')$ diagram for period-2 orbits.

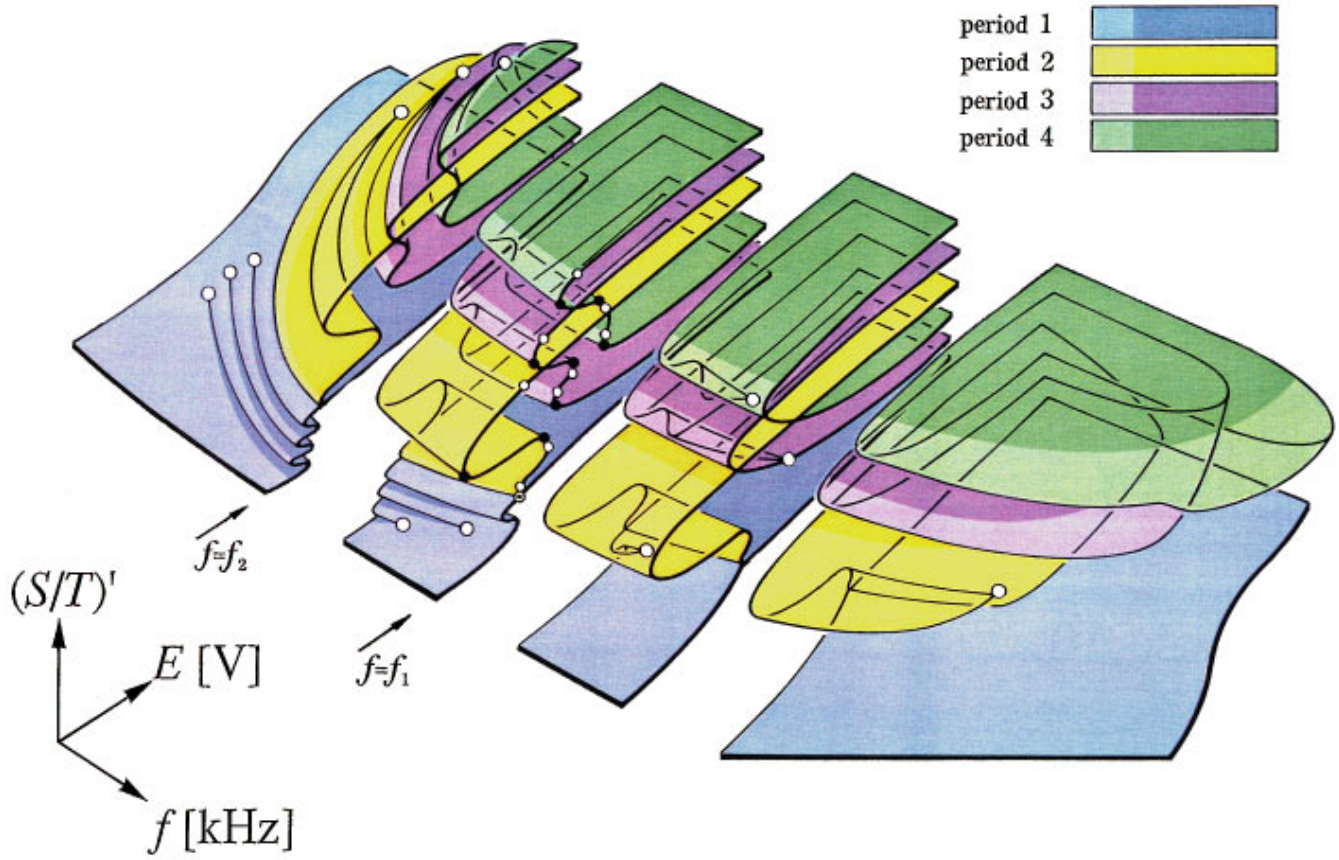

FIG. 23. A schematic model $(f,E,(S/T)')$ diagram for all the periodic orbits. The following color code is used. Blue: period 1. Yellow: period 2. Purple: period 3. Green: period 4.

indicates stable periodic orbits; the dark colored region stands for unstable periodic orbits. (Due to the color printing process, the dark yellow and light yellow may not be distinguishable.) The large white circles are the cusp points of the saddle node bifurcation sets. The small black (white) circles on the section of the figures show the saddle node bifurcation points (period doubling bifurcation points). The small white circle with a dot shows period doubling bifurcation point of period 1. These pictures completely clarify those points explained in Sec. I. In particular, the following are true.

(1) The period-1 attractors which are repeatedly observed constitute a sheet structure in $(f,E,S/T)$ space, and hence their associated unstable period-1 orbits belong to the same (blue) family.

(2) Other periodic attractors of the same periods and their associated unstable periodic orbits form a sheet structure, and therefore belong to the same families (green, purple, or yellow).

Let us now check how well this global picture captures the experimentally observed data in terms of Figs. 2, 3, and 23. The experimental result in Fig. 2(a) corresponds to the cross section of Fig. 23 indicated by $f=f_1$, which is redrawn in Fig. 2(b) in order to make the correspondence transparent. In Fig. 2(a) the stable orbits are indicated by the thick lines; in Fig. 23, stable orbits are indicated by lighter colors. Figure 3(a) corresponds to the part of the cross section of Fig. 23 indicated by $f=f_2$, where the wavy blue sheet is seen at the small E values. In Fig. 3(b), the stable orbits are drawn as thick lines. Also indicated in Fig. 3(b) are the saddle node bifurcation points (black dots) and the period doubling bifurcation sets (white circles). These bifurcation sets are not drawn at the $f=f_2$ cross section of Fig. 23 in order to avoid complication. The correspondence between the experimental and analytical results is clear.

VI. CONCLUSION

A global bifurcation analysis was made of a driven R-L-diode circuit. This paper has clarified most of the global bifurcation structure observed in the circuit by deriving exact bifurcation equations then drawing the diagrams in $(f,E,S/T)$ space instead of on the (f,E) plane. The major findings are as follows.

(i) The repeatedly observed period-1 attractors and their associated unstable period-1 orbits constitute a sheet structure in $(f,E,S/T)$ space, and hence belong to the same family of period-1 orbits.

(ii) The two different period three windows (A_3 and B_3 in Fig. 2) are born out of two different saddle node bifurcations, and yet they belong to the same family of period-3 orbits.

(iii) The same is true for A_4 and B_4 in Fig. 2, i.e., the two different period-4 windows.

(iv) The situation is different for A_2 and B_2 in Fig. 2, i.e., the two different period-2 intervals. The stable period-2 interval A_2 is born out of a period doubling bifurcation of a period-1 orbit, while window B_2 is the result of a saddle node bifurcation, and yet they belong to the same family of period-2 orbits.

(v) A global perspective which is consistent with the experimentally observed data is clarified. Very good correspondence between the numerical and experimental results is obtained.

ACKNOWLEDGMENTS

The authors would like to thank M. Komuro from Teikyo Science University, R. Tokunaga from Tsukuba University and J. Noguchi from Waseda University for many constructive discussions. Thanks are also due to M. Nakai of Kyoto University for bringing to our attention a similarity between the R-L-diode circuit and the gear meshing vibration.

[1] M. J. Feigenbaum, Los Alamos Sci. **1**, 4 (1980).
[2] Y. Pomeau and P. Manneville, Commun. Math. Phys. **74**, 189 (1980).
[3] C. Grebogi, E. Ott, and J. A. Yorke, Phys. Rev. Lett. **48**, 1507 (1982).
[4] P. S. Linsay, Phys. Rev. Lett. **47**, 1349 (1981).
[5] J. Testa, J. Perez, and C. Jeffries, Phys. Rev. Lett. **48**, 714 (1982).
[6] R. W. Rollins and E. R. Hunt, Phys. Rev. Lett. **49**, 1295 (1982).
[7] S. D. Bronson, D. Dewey, and P. S. Linsay, Phys. Rev. A **28**, 1201 (1983).
[8] H. Ikezi, J. S. deGrassie, and T. H. Jenson, Phys. Rev. A **28**, 1207 (1983).
[9] J. Cascais, R. Dilao, and A. Norondacosta, Phys. Lett. **93A**, 213 (1983).
[10] D. Azzouz, R. Duhr, and M. Hasler, IEEE Trans. CAS **30**, 913 (1983).
[11] E. R. Hunt and R. W. Rollins, Phys. Rev. A **29**, 1000 (1984).
[12] T. Klinker, W. M. Ilse, and W. Lauterborn, Phys. Lett. **101A**, 371 (1984).
[13] M. F. Bocko, D. H. Douglass, and H. Frutchy, Phys. Lett. **104A**, 388 (1984).
[14] D. Azzouz, R. Duhr, and M. Hasler, IEEE Trans. CAS **31**, 1155 (1984).
[15] T. Matsumoto, L. O. Chua, and S. Tanaka, Phys. Rev. A **30**, 1155 (1984).
[16] T. H. Yoon, J. W. Song, S. Y. Shin, and J. W. Ra, Phys. Rev. A **30**, 3347 (1984).
[17] C. D. Jeffries, Phys. Scr. **T9**, 11 (1985).
[18] S. Tanaka, T. Matsumoto, and L. O. Chua, Proc. IEEE ISCAS, 851 (1985).
[19] J. M. Perez, Phys. Rev. A **32**, 2990 (1985).
[20] J. Mevissen, R. Seal, and L. Waters, Phys. Rev. A **32**, 2990 (1985).
[21] S. Tanaka, T. Matsumoto, and L. O. Chua, Physica D **28**, 317 (1987).
[22] J. H. Baxter, M. F. Bocko, and D. H. Douglass, Phys. Rev. A **41**, 619 (1990).
[23] S. Tanaka, T. Matsumoto, J. Noguchi, and L. O. Chua, Phys. Lett. **157A**, 37 (1991).
[24] S. Tanaka, J. Noguchi, S. Higuchi, and T. Matsumoto, IEICE Trans. **74**, 1406 (1991).
[25] S. Higuchi, S. Tanaka, M. Komuro and T. Matsumoto, in *Advanced Series in Dynamical Systems*, edited by H. Kawakami

(World Scientific, Singapore, 1991), Vol. 10, pp. 119–138.
[26] T. Matsumoto, M. Komuro, H. Kokubu, and R. Tokunaga, *Bifurcations: Sights, Sounds and Mathematics* (Springer-Verlag, Tokyo, 1993).
[27] M. Kuroda, T. Hikawa, and M. Nakai, Trans. JSME **61**, 815 (1995).
[28] M. Kuroda, Y. Matsui, and M. Nakai, Trans. JSME **61**, 808 (1995).
[29] J. M. T. Thompson, Proc. R. Soc. London Ser. A **387**, 407 (1983).
[30] E. R. Hunt, Phys. Rev. Lett. **67**, 1953 (1991).
[31] T. Matsumoto and N. Nishi (unpublished).
[32] E. S. Yang, *Fundamentals of Semiconductor Devices* (McGraw-Hill, New York, 1987).
[33] H. C. Poon, and H. K. Gummel, Proc. IEEE **57**, 2181 (1969).
[34] B. R. Chawla and H. K. Gummel, IEEE Trans. Electron Devices **ED-18**, 178 (1971).